Catalysis Today 160 (2011) 61–69

Contents lists available at ScienceDirect

Catalysis Today

journal homepage: www.elsevier.com/locate/cattod

# Low-temperature 1,3-butadiene hydrogenation over supported Pt/3d/γ-$Al_2O_3$ bimetallic catalysts☆

William W. Lonergan, Xianjie Xing, Renyang Zheng, Suitao Qi, Benjamin Huang, Jingguang G. Chen*

*Department of Chemical Engineering, Center for Catalytic Science and Technology (CCST), University of Delaware, Newark, DE 19716, USA*

ARTICLE INFO

*Article history:*
Available online 17 June 2010

*Keywords:*
Bimetallic catalysts
Platinum
Cobalt
Nickel
Copper
Hydrogenation
1,3-Butadiene

ABSTRACT

Low-temperature 1,3-butadiene hydrogenation is used as a probe reaction to investigate the hydrogenation activity over several γ-$Al_2O_3$ supported Pt/3d (3d = Co, Ni, Cu) bimetallic catalysts. Batch and flow reactor studies are employed to quantify the kinetic activity and steady-state conversion, respectively, of each catalyst. Transmission electron microscopy (TEM) is utilized to characterize particle sizes and extended X-ray absorption fine structure (EXAFS) measurements are performed to verify the Pt–3d bimetallic bond formation. Pulse carbon monoxide chemisorption measurements are also performed to characterize the number of active sites. Additionally, density functional theory (DFT) calculations are included to determine the binding energies of 1,3-butadiene and atomic hydrogen on the corresponding model surfaces. The binding energies of the adsorbates are found to correlate with the hydrogenation activity, allowing for use of such correlation to potentially predict hydrogenation catalysts with enhanced activity based on the binding energies of the adsorbates of interest.



## 1. Introduction

Bimetallic catalysts are known to often exhibit novel properties that differentiate them from the corresponding monometallic catalysts [1,2]. Many research groups have attempted to gain a better understanding for these properties in order to predict and design bimetallic catalysts in many applications [3–5]. Early findings have illustrated that the catalytic properties of bimetallic catalysts can be tuned by adjusting the relative amounts of the two metals [1]. In recent years, many fundamental investigations incorporating both experimental studies and theoretical calculations have been performed in an attempt to correlate the electronic properties of bimetallic surfaces with their catalytic properties [2,6–14].

Many recent investigations on bimetallic surfaces have found that the structure of the surfaces greatly affects both the electronic and catalytic properties [7,9,12,13,15–17]. Pt/3d-metal systems have been bimetallic surfaces of interest in many investigations due to both their novel properties and the potential to decrease the Pt loading by the addition of a less expensive 3d-metal. Recent experimental work in our group has focused on the Ni/Pt(1 1 1) and Co/Pt(1 1 1) monolayer bimetallic systems [15,18–20], while parallel theoretical calculations have been used to further understand these surfaces and also to predict additional bimetallic combinations with specific catalytic properties [17,21–23]. In the case of the Ni/Pt(1 1 1) or Co/Pt(1 1 1) monolayer bimetallic system it was discovered that the 3d-metal (either Ni or Co) monolayer can be located either on the surface, yielding a 3d-terminated 3d–Pt–Pt(1 1 1) surface, or in the subsurface region, yielding a Pt-terminated Pt–3d–Pt(1 1 1) subsurface structure [15,18,19]. The surface and subsurface structures exhibit unique properties that differ from each other and from either monometallic surface [13,15,16,24]. The Pt–3d–Pt(1 1 1) surface binds atomic hydrogen and alkenes more weakly than the 3d–Pt–Pt(1 1 1) and monometallic surfaces, leading to a novel low-temperature hydrogenation pathway on the Pt–3d–Pt(1 1 1) subsurface structure [17,20]. However, the 3d–Pt–Pt(1 1 1) structure binds adsorbates more strongly than the Pt–3d–Pt(1 1 1) and monometallic surfaces [16], making it more active toward the reforming of oxygenates, such as ethylene glycol and glycerol to produce $H_2$ and CO [16,25]. The differences in binding energies on the two novel bimetallic surfaces have also been explored theoretically using density functional theory (DFT) calculations. The activity trends observed in experimental studies were also supported by the binding energies and d-band centers calculated through the DFT methods [6,21,22].

Another interesting feature of novel bimetallic surfaces is that, for a given bimetallic system, the thermodynamically stable structure depends on the nature of the adsorbates [22]. Through both experimental and theoretical studies, it has been observed that the Pt–3d–Pt(1 1 1) subsurface structure is stable either in vacuum or with adsorbed atomic hydrogen [22], however, if this surface is exposed to oxygen, the 3d-metal atoms segregate to the surface to

☆ This paper is for a special issue entitled "Heterogeneous Catalysis by Metals: New Synthetic Methods and Characterization Techniques for High Reactivity" guest edited by Jinlong Gong and Robert Rioux.

* Corresponding author.
*E-mail address:* jgchen@udel.edu (J.G. Chen).

0920-5861/$ – see front matter © 2010 Elsevier B.V. All rights reserved.
doi:10.1016/j.cattod.2010.05.014

create the 3d–Pt–Pt(1 1 1) structure [19,26]. It is important to note that the activation barrier for the transformation between subsurface and surface structures is only ~15 kcal/mol for Pt–Ni–Pt(1 1 1) and ~7 kcal/mol for Pt–Co–Pt(1 1 1) [19], suggesting that the 3d-metal atoms may diffuse and segregate during calcination and reduction procedures as well as under reaction conditions. Similar behavior has been reported in recent in situ studies on both polycrystalline foils [27] and supported catalysts [28], where Ni atoms in Pt/Ni catalysts were observed to segregate from the subsurface to surface in the presence of oxygen, with the reverse process occurring in the presence of hydrogen.

In a recent study on supported Pt/Ni catalysts two series of catalysts were characterized to understand the effects of metal atomic ratio and impregnation sequence on the catalyst structure and activity toward low-temperature hydrogenation [29]. From FTIR spectroscopy of adsorbed carbon monoxide (CO), it was observed that CO bound through Pt atoms on all the catalysts after hydrogen reduction, suggesting that the surfaces of the supported nanoparticles were primarily Pt-terminated and that Ni atoms were mostly beneath the surface. In testing these catalysts for low-temperature hydrogenation activity it was observed that all of the bimetallic catalysts outperformed monometallic catalysts. The results from CO adsorption and reactor evaluation strongly suggested that the enhanced activity observed over the supported Pt/Ni bimetallic catalysts could be due to surface Pt atoms modified by subsurface Ni in nanoparticles, similar to how the structure of the Pt–Ni–Pt(1 1 1) monolayer bimetallic surface allowed for novel activity [29].

The objective of the current paper is to extend the correlation between monolayer bimetallic surfaces and supported Pt/Ni catalysts to additional Pt/3d-metal bimetallic catalysts. For this work PtCo/$\gamma$-$Al_2O_3$, PtNi/$\gamma$-$Al_2O_3$, and PtCu/$\gamma$-$Al_2O_3$ bimetallic catalysts were synthesized with Pt:3d atomic ratios of 1:10 using a co-impregnation procedure, which was determined to be better than sequential impregnation in our previous study [29]. Extended X-ray absorption fine structure (EXAFS) and transmission electron microscopy (TEM) were used to characterize the extent of bimetallic formation and particle size, respectively. Batch and flow reactor studies of low-temperature 1,3-butadiene hydrogenation were performed in order to understand how the structure of the bimetallic catalysts influenced the hydrogenation activity.

The reaction of 1,3-butadiene hydrogenation is of practical importance in removing impurities from the butene stream produced from the cracking of naphtha or gas oil. For the successful polymerization of butene, 1,3-butadiene must be removed from the feed stream, since only very small amounts of 1,3-butadiene (up to 1%) are sufficient to poison the polymerization catalysts [30]. Pd-[31–33] and Pt-based [34,35] bimetallic catalysts are commonly studied for use in 1,3-butadiene hydrogenation. Pd catalysts are reported to be the most active and selective catalysts for the selective hydrogenation of dienes [36], but some literature has shown that Pt/3d and Pd/3d bimetallic catalysts may also display both high activity and selectivity to 1,3-butadiene hydrogenation [34,36].

## 2. Experimental

### 2.1. Catalyst preparation

A slurry-based impregnation was used to synthesize $\gamma$-$Al_2O_3$ supported catalysts in this study. A 1.7 wt.% of Pt/$\gamma$-$Al_2O_3$ catalyst was synthesized to serve as a control, while the three bimetallic catalysts were all synthesized to have a Pt:3d-metal atomic ratio of 1:10. Table 1 lists the catalysts and their nominal metal loadings.

The synthesis was carried out by dissolving the metal precursor salts in excess water (15 mL $H_2O$ per gram of catalyst) and then adding $\gamma$-$Al_2O_3$ to the solution. The solution was sonicated for 1 h and then dried at 373 K for 24 h and calcined at 563 K for 2 h. The precursor salts used in this study were: $Pt(NH_3)_4(NO_3)_2$, $Co(NO_3)_2{\cdot}6H_2O$, $Ni(NO_3)_2{\cdot}6H_2O$, $Cu(NO_3)_2{\cdot}xH_2O$, all purchased from Alfa Aesar.

### 2.2. Catalyst characterization

#### 2.2.1. Pulse CO chemisorption

Carbon monoxide (CO) uptake and metal dispersion were determined using an Altamira Instruments AMI-200ip to perform pulse CO chemisorption measurements. The details of this procedure have been reported previously [29]. In brief the catalysts were reduced at 723 K under a hydrogen–helium mixture before performing pulse CO chemisorptions at room temperature. A stoichiometry of M:CO = 1:1 (M = Pt, Co, Ni, Cu) was assumed in order to estimate the metal dispersion from the chemisorption measurements.

#### 2.2.2. Transmission electron microscopy

TEM imaging was performed to characterize the particle size of the reduced bimetallic catalysts using a JEOL 2010F equipped with a Schottky field emission gun operated at 200 keV, with an ultra-high resolution pole piece providing a point resolution of 1.9 Å. High-angle annular dark field (HAADF) imaging was used to increase the contrast between the metal particles and the $\gamma$-$Al_2O_3$ support. An EDAX Phoenix X-ray spectrometer was used to perform elemental analysis. Both HAADF imaging and energy dispersive X-ray spectroscopy (EDS) were performed in scanning mode (STEM) using a 20 nm camera length and a 0.5 nm diameter nanoprobe. Samples for TEM imaging were prepared by grinding and suspending catalysts in ethanol, from which a small amount of the solution was dropped onto either a copper or gold grid coated with a lacey carbon. The grids were allowed to dry before loading the samples into the TEM.

#### 2.2.3. Extended X-ray absorption fine structure (EXAFS)

EXAFS measurements of the Pt $L_{III}$-edge were collected in order to detect and characterize the formation of Pt–3d bimetallic bonds. These measurements were made on the X19A Beamline at the National Synchrotron Light Source (NSLS), Brookhaven National Laboratory. The procedures for EXAFS sample preparation and data collection have been previously reported [29]. Catalyst pellets were reduced at 723 K under a constant flow of hydrogen and helium before collecting EXAFS measurements at room temperature.

The EXAFS measurements were analyzed using the IFFEFIT 1.2.11 data analysis package (Athena, Artemis, Atoms, and FEFF6) [37,38]. Multiple scans were taken for each sample, and the raw data were reduced in Athena by aligning the individual scans to the foil standard, deglitching when necessary, and merging multiple scans together to reduce experimental error. The isolated-atom background function was removed in Athena using the AUTOBK algorithm and then the data were Fourier transformed into R-space where Artemis was used to obtain local structural information by fitting each data set with theoretical standards generated by FEFF6 [39]. In fitting the data for the bimetallic catalysts, both the Pt–Pt and Pt–3d contributions to the theoretical EXAFS were taken into account. The theoretical Pt–Pt photoelectron amplitudes and phases were calculated for the bulk Pt fcc structure. The Pt–3d contributions were modeled by replacing Pt with the appropriate 3d-metal (Co, Ni, or Cu) in the first nearest neighbor shell. The passive electron reduction factor ($S_0^2$) was found to be 0.85 from fitting the Pt foil data, and this value was fixed throughout the fitting of all the catalysts. Seven parameters were used in fitting the data. These parameters were: the correction to the edge energy, the coordination numbers of the Pt–Pt and Pt–3d bonds, corrections to their model inter-atomic distances, and their mean-square deviations in inter-atomic distances (EXAFS Debye–Waller factors).

**Table 1**
Catalyst compositions and nomenclature.

| Catalyst | Metal content (wt.%) | | Atomic ratio (Pt:3d) | Nomenclature | CO uptake (μmol CO/g catalyst) | Dispersion (%) |
|---|---|---|---|---|---|---|
| | Pt | 3d | | | | |
| 1.7%Pt/γ-$Al_2O_3$ | 1.7 | – | – | Pt/γ-$Al_2O_3$ | 38.9 | 45.4 |
| 1.7%Pt–5.0%Co/γ-$Al_2O_3$ | 1.7 | 5.0 | 1:10 | PtCo/γ-$Al_2O_3$ | 46.5 | 13.6 |
| 1.7%Pt–5.0%Ni/γ-$Al_2O_3$ | 1.7 | 5.0 | 1:10 | PtNi/γ-$Al_2O_3$ | 97.0 | 28.4 |
| 1.7%Pt–5.4%Cu/γ-$Al_2O_3$ | 1.7 | 5.4 | 1:10 | PtCu/γ-$Al_2O_3$ | 34.9 | 9.6 |

### 2.3. Catalytic evaluation

#### 2.3.1. FTIR batch reactor studies

Fourier transform infrared (FTIR) spectroscopy was used to follow the concentrations of reactants and products during the low-temperature hydrogenation of 1,3-butadiene within a batch reactor system. The design of the IR cell was based on a design reported elsewhere in the literature [40], and the procedures for sample preparation and 1,3-butadiene hydrogenation have been previously reported [29]. The stainless steel IR cell, fitted with infrared-transparent $BaF_2$ windows, allowed for in situ reduction of catalysts and spectroscopic measurements of either surface adsorbates or gas-phase species. Spectra were recorded with 4 $cm^{-1}$ resolution using a Thermo Nicolet Nexus 470 spectrometer equipped with a MCT-A (mercury cadmium telluride) detector.

Intensity–concentration relationships were obtained for the reactant and products so their concentrations could be accurately calculated during the hydrogenation reaction. These relationships were determined by measuring the intensity of each peak at a number of pressures in a range relevant to the reaction. Using the volume of the reactor and the ideal gas law, gas-phase concentrations were calculated based on the pressure–intensity correlation for each molecule.

The concentration of 1,3-butadiene was followed using the peak intensity of the vibrational mode at 1586 $cm^{-1}$ (C=C–C=C stretching mode). 1-Butene was found to be the only butene molecule produced because no peaks corresponding to cis-2-butene were observed, which strongly suggested that no trans-2-butene was present either, since it would be expected for the two isomers to be under thermodynamic equilibrium. In the absence of 2-butenes, the concentration of 1-butene was calculated using the intensity of the vibrational mode at 1655 $cm^{-1}$ (C=C stretching). Because n-butane does not have any characteristic peaks that do not overlap with peaks from other molecules its concentration was estimated with Eq. (1)

$$\text{Intensity}_{\text{Butane(1466)}} = \text{Intensity}_{\text{Total(1466)}} - \text{Conc}_{\text{1-Butene(1655)}} \times \left( \frac{\text{Intensity}_{\text{1-Butene(1466)}}}{\text{Conc}_{\text{1-Butene(1466)}}} \right) \quad (1)$$

where by calculating the intensity of 1-butene at 1466 $cm^{-1}$ ($CH_3$ deformation) and subtracting that from the total intensity at 1466 $cm^{-1}$, the resulting intensity corresponding to n-butane is obtained.

#### 2.3.2. Flow reactor studies

The hydrogenation of 1,3-butadiene was also investigated in a fixed bed flow reactor under atmospheric pressure at 308 K. For each experiment, 15 mg of fresh catalyst was loaded into the flow reactor. Prior to reaction, the catalysts were reduced in a $H_2$ (20 sccm) and He (20 sccm) mixture at 723 K for 1 h. The temperature of the catalyst was linearly ramped at a rate of 14 K/min until the reduction temperature was reached. Following reduction, the catalyst was exposed to the reactant gas flows. The composition of the gas-phase reactant flow as a mixture of 3.12% 1,3-butadiene and 6.25% $H_2$ balanced with He. The total gas flow rate was 160 sccm. The products were analyzed by online gas chromatography (HP 5890) equipped with a flame ionization detector (FID) and a HP-Plot Alumina column. Peak areas were calibrated using a certified gas mixture of 1,3-butadiene, 1-butene, trans-2-butene, cis-2-butene, and n-butane (1000 ppm each) balanced with He.

### 2.4. Density functional theory calculations

DFT calculations were performed with the Vienna Ab initio Simulation Package (VASP) [41–43]. The PW 91 functional [44] was applied in the generalized gradient approximation (GGA) [45] calculation and a kinetic energy cutoff of 396 eV for the plane wave truncation was used. A periodic 3 × 3 unit cell structure was modeled using four layers of metal added by six equivalent layers of vacuum. For the four layers of metal, the bottom two layers were frozen with the Pt metal distance of 2.83 Å, while the top two layers were allowed to relax to reach the lowest energy configuration. 1,3-Butadiene was placed onto the surface in the 1,2,3,4-tetra-σ orientation, which was found to be the most stable orientation reported in the literature [36], with an initial adsorbate–surface bond distance of 2 Å.

The binding energy (*BE*) of adsorbate *A* is related to the interaction between the surface and the adsorbate, and is calculated using the following equation [22]:

$$BE_{A/slab} = n \cdot E_{A/slab} - n \cdot E_{slab} - E_{A_n(g)} \quad (2)$$

where $E_{A/slab}$ is the total energy of the slab plus the adsorbate, $E_{slab}$ is the energy of the bare slab, $E_{A_n(g)}$ is the energy of the gas-phase adsorbate and *n* is the number of adsorption sites needed per adsorbate. The surface d-band center value was used to correlate *BE* values, and was calculated using standard procedures described previously [6].

## 3. Results

### 3.1. CO chemisorption measurements

Table 1 lists both the CO uptake and metal dispersion results. For bimetallic catalysts there is uncertainty in the surface composition of the catalyst particles, therefore the dispersion values listed in Table 1 may not be physically meaningful but they are listed to provide a relative ranking of overall metal dispersion. On the other hand, the value of CO uptake provides a more quantitative comparison of the number of active sites between the catalysts.

The values in Table 1 show that the dispersion follows the order Pt/γ-$Al_2O_3$ > PtNi/γ-$Al_2O_3$ > PtCo/γ-$Al_2O_3$ > PtCu/γ-$Al_2O_3$. Since the Pt/γ-$Al_2O_3$ catalyst has a lower total metal loading than the other three bimetallic catalysts, it is expected to have a smaller particle size. The values of CO uptake follow a different order than dispersion: PtNi/γ-$Al_2O_3$ > PtCo/γ-$Al_2O_3$ > Pt/γ-$Al_2O_3$ > PtCu/γ-$Al_2O_3$. The PtNi/γ-$Al_2O_3$ and PtCo/γ-$Al_2O_3$ catalysts have larger CO uptake values than Pt/γ-$Al_2O_3$ because there are more adsorption sites due to the presence of additional Ni and Co

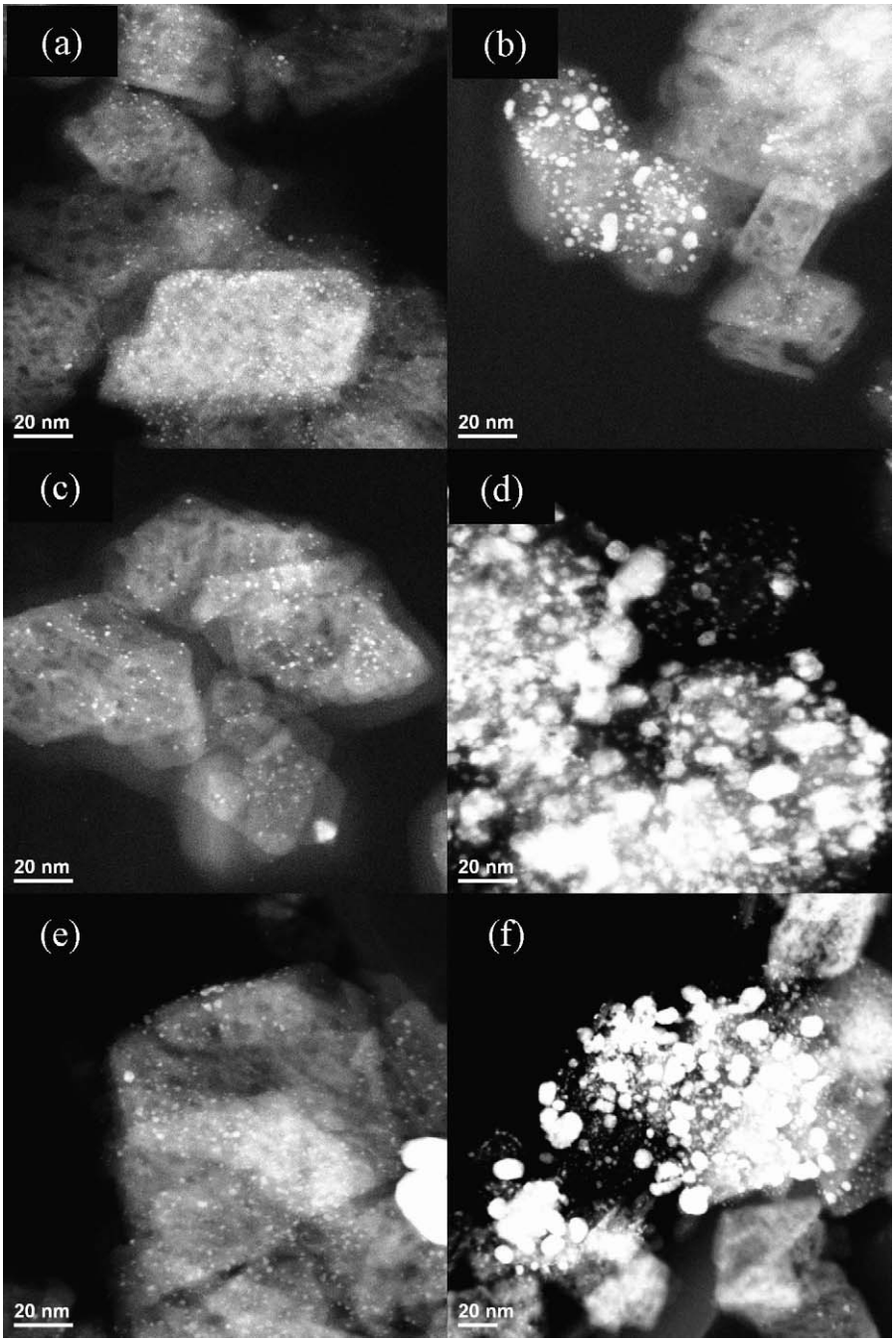


**Fig. 1.** HAADF TEM images and particle size distributions of bimetallic catalysts: (a,b) PtCo/γ-$Al_2O_3$, (c,d) PtNi/γ-$Al_2O_3$, and (e,f) PtCu/γ-$Al_2O_3$.

metal atoms, respectively. In contrast, the uptake value of PtCu/γ-$Al_2O_3$ is slightly lower than Pt/γ-$Al_2O_3$, suggesting that Cu does not adsorb CO at room temperature.

### 3.2. TEM imaging

TEM images collected in high-angle annular dark field (HAADF) mode are shown in Fig. 1. As seen in the images, there appears to be a bimodal distribution of particle sizes in each of the bimetallic catalysts. The dominant population in each catalyst appears to be the smaller particles (Fig. 1a, c, and e), which range in diameter from approximately 1 nm to 3 nm. EDS analysis (spectra not shown) was performed on some of the larger particles and revealed the presence of both Pt and the 3d-metals.

### 3.3. EXAFS results

The Pt $L_{III}$-edge XANES spectra for the three bimetallic catalysts are shown both before and after reduction in Fig. 2, along with the Pt foil spectra for reference. Fig. 3 shows the background-subtracted, edge-step normalized and $k^2$-weighted Pt $L_{III}$-edge EXAFS data ($\chi(k)$) in R-space. In performing the Fourier transform of the data, a Hanning window function with sill width $\Delta k = 2\,\text{Å}^{-1}$ was applied to a $k$-range from $2\,\text{Å}^{-1}$ to $16\,\text{Å}^{-1}$.

Information regarding the oxidation state of Pt can be obtained from the examination of the XANES spectra [46] in Fig. 2 along with the Fourier transformed EXAFS data in Fig. 3. The XANES results show that before reduction in hydrogen the catalysts exhibit large white-line features that disappear after reduction. The presence

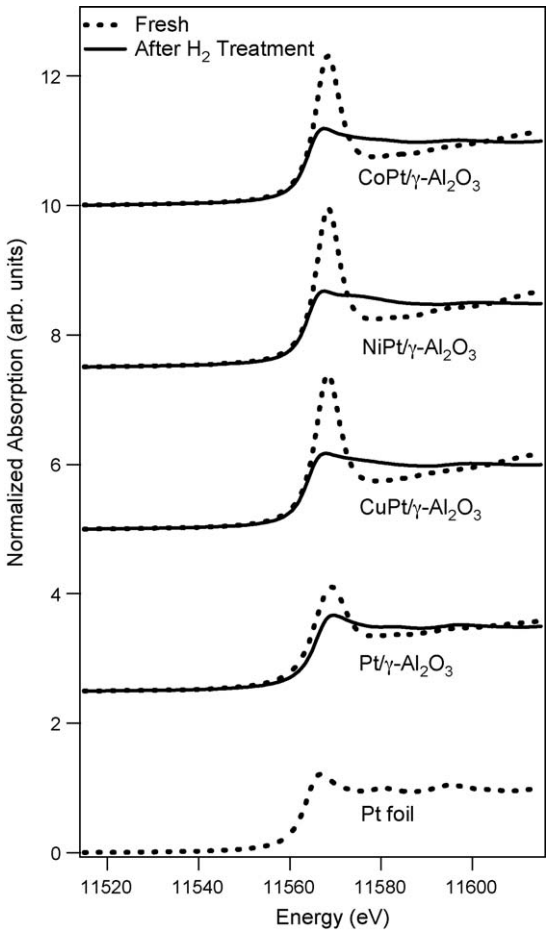


**Fig. 2.** Pt $L_{III}$-edge XANES spectra before and after reduction. The Pt foil is included to serve as a reference for metallic Pt.

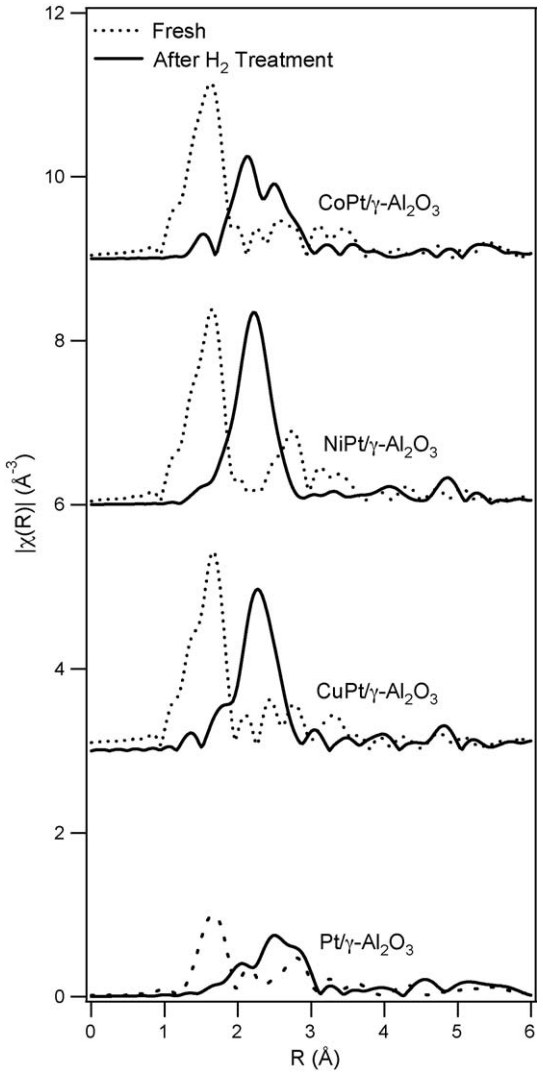


**Fig. 3.** Fourier transformed (magnitude) $k^2$-weighted EXAFS function ($\chi(k)$) of Pt $L_{III}$-edge before and after reduction.

of the white-line feature before reduction can be attributed to the higher density of unoccupied d-states of oxidized Pt, while the lack of the feature after reduction suggests that Pt atoms have been reduced to the metallic state. The Pt $L_{III}$-edges after reduction appear very similar to the Pt foil, which serves as further proof that Pt has been reduced in all the bimetallic catalysts. Similarly the EXAFS data in Fig. 3 can also be used to draw conclusions about the oxidation state of Pt in the catalyst nanoparticles. Large peaks at low radial distribution ($R < 2$ Å), attributed to Pt–O bonds, appear for all catalysts before reduction. After reduction, the Pt–O peaks disappear and are replaced by Pt–M (M = Pt or 3d-metal) peaks that appear at slightly larger values of R ($2 < R < 3$ Å).

Fig. 4 shows the Fourier transformed EXAFS data after reduction and the fits to the first coordination shell obtained using FEFF6 theory [39]. Table 2 summarizes the results of the EXAFS data fitting. The EXAFS data for the bimetallic catalysts were analyzed by including both Pt–Pt and Pt–3d contributions; Pt–O contributions were neglected in the fitting of the reduced catalysts based on the conclusion of complete Pt reduction in Figs. 2 and 3. For bulk metals the Co–Co, Ni–Ni, Cu–Cu, and Pt–Pt distances are 2.51 Å, 2.49 Å, 2.55 Å, and 2.77 Å, respectively. If the metals in the catalysts were to segregate into monometallic nanoparticles, it would be expected that their first nearest neighbor distance would be similar or slightly smaller than the bulk distances, with the latter being due to the particle size effect on inter-atomic distance. If the metals were to form bimetallic particles, then the Pt–3d nearest neighbor distance should be an intermediate value between the two monometallic distances. The fitting results in Table 2 show that the Pt–Co, Pt–Ni, and Pt–Cu distances in the bimetallic catalysts are 2.56 Å, 2.55 Å, and 2.60 Å, respectively. These distances are consistent with the formation of bimetallic bonds, because they fall between the bulk 3d–3d and Pt–Pt distances. The Pt–Pt inter-atomic distances presented in Table 2 are also of interest because they are smaller than that for the monometallic Pt/$\gamma$-$Al_2O_3$. In a previous study on Pt/Ni bimetallic catalysts, it was also observed that the Pt–Pt inter-atomic distances in bimetallic catalysts were significantly smaller than the Pt–Pt distance in monometallic Pt catalysts [29]. The smaller Pt–Pt distances observed in the bimetallic catalysts in Table 2 suggest that the Pt atoms are in a strained state due to the lattice mismatch between the 3d-metal atoms and the Pt atoms. One possible structure that would place Pt atoms under a similar compressive strain would be a monolayer of Pt atoms on top of a 3d-metal nanoparticle.

In addition to determining the Pt–3d inter-atomic distances, the Pt–3d coordination numbers can also be used to verify the presence of Pt–3d bimetallic bonds and quantify the extent of bimetallic bond formation. Table 2 shows that the Pt–3d coordination numbers are 3.3, 6.8, and 6.3 for the PtCo/$\gamma$-$Al_2O_3$, PtNi/$\gamma$-$Al_2O_3$, and PtCu/$\gamma$-$Al_2O_3$ catalysts, respectively, confirming the presence of bimetallic bonds. The comparison also suggests that the extent of Pt–3d formation is less in PtCo/$\gamma$-$Al_2O_3$ than in the other two bimetallic catalysts.

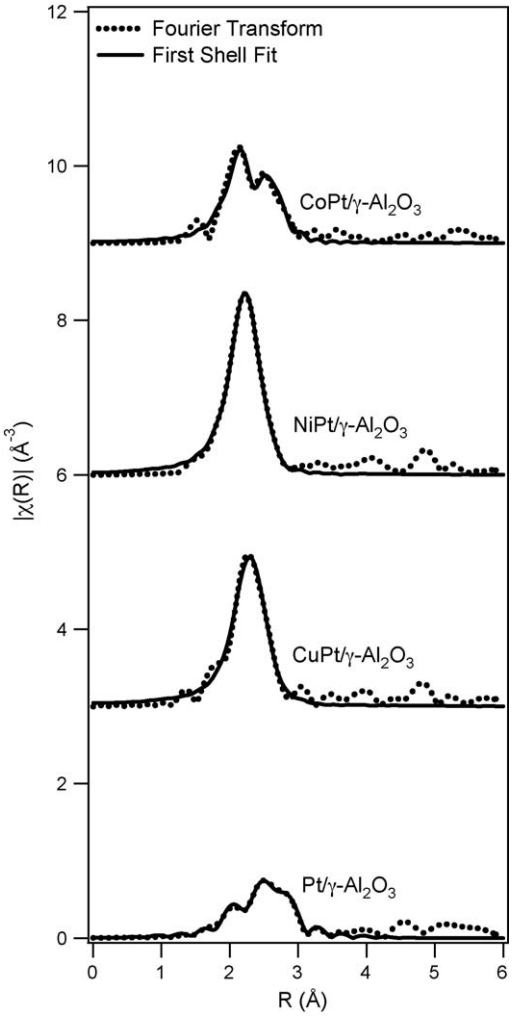


**Fig. 4.** Fourier transformed (magnitude) $k^2$-weighted EXAFS function ($\chi(k)$) and fitted data of Pt $L_{III}$-edge of the catalysts after reduction. Transformed data and fits are shown as dashed and solid lines, respectively.

Using a correlation proposed by Frenkel et al., the coordination numbers obtained from the EXAFS analysis can be used to predict particle size [47]. Assuming a hemispheric geometry, this correlation predicts average particle sizes of approximately 1.8 nm, 2.6 nm, and 3.3 nm for the PtCo/γ-$Al_2O_3$, PtNi/γ-$Al_2O_3$, and PtCu/γ-$Al_2O_3$ catalysts, respectively. EXAFS is a volume averaged technique, therefore the presence of large particles would dominate the signal. The fact that this correlation predicts particle sizes that agree well with the population of small particles, as observed in TEM, suggests that the small particles far outnumber the larger ones.

### 3.4. FTIR batch reactor studies

Fig. 5a–c shows the rates of consumption of 1,3-butadiene, production and subsequent consumption of 1-butene, and production of n-butane, respectively. The primary goal of this set of experiments was to compare the hydrogenation rate of 1,3-butadiene, but the product selectivity is also of interest over the different bimetallic catalysts. Fig. 5a illustrates that all three of the bimetallic catalysts are more active to 1,3-butadiene hydrogenation than monometallic Pt/γ-$Al_2O_3$, With PtCu/γ-$Al_2O_3$ showing the lowest activity among the three bimetallic catalysts. Gas-phase 1-butene (Fig. 5b) is not detected over the PtNi/γ-$Al_2O_3$ and PtCo/γ-$Al_2O_3$ catalysts, indicating that these two catalysts are very active toward the complete hydrogenation of both C=C bonds in 1,3-butadiene. In comparison, both PtCu/γ-$Al_2O_3$ and Pt/γ-$Al_2O_3$ show the production of a significant amount of gas-phase 1-butene. Fig. 5c compares the concentration of gas-phase n-butane over the different catalysts, indicating that the trend in the production rate of n-butane is consistent with the trend in the consumption rate of 1,3-butadiene (Fig. 5a).

As shown in the overall carbon balance in Fig. 5d, satisfactory gas-phase carbon balances were obtained for the PtNi/γ-$Al_2O_3$ and PtCo/γ-$Al_2O_3$ catalysts. However, PtCu/γ-$Al_2O_3$ displayed a relatively poor carbon balance among all the catalysts. Since no 2-butenes were observed in the gas-phase FTIR spectra, it is most likely that a fraction of the intermediates adsorbed on the PtCu/γ-$Al_2O_3$ catalyst.

In order to make quantitative comparisons between catalysts, the rate of 1,3-butadiene hydrogenation was estimated by fitting the experimental data with first-order kinetics of the consumption of 1,3-butadiene. These rate constants are listed in Table 3 along with rate constants normalized to the CO uptake per milligram of catalyst obtained from CO chemisorption measurements. From the rate constants listed in the first column in Table 3 it can be seen that, on the basis of catalyst weight, the rate constant follows the order of PtNi/γ-$Al_2O_3$ > PtCo/γ-$Al_2O_3$ > PtCu/γ-$Al_2O_3$ > Pt/γ-$Al_2O_3$. After normalizing the rate constants by the CO uptake, the trend in the rate constants changes to PtCo/γ-$Al_2O_3$ > PtNi/γ-$Al_2O_3$ > PtCu/γ-$Al_2O_3$ > Pt/γ-$Al_2O_3$. The only difference between using the two types of rate constants is that the order is reversed for the PtNi/γ-$Al_2O_3$ and PtCo/γ-$Al_2O_3$ catalysts.

**Table 3**
First order consumption rate constants for 1,3-butadiene hydrogenation obtained from batch reactor studies.

| Catalyst | $k$ ($min^{-1}$ g $cat^{-1}$) | $k$ (normalized to CO uptake, $min^{-1}$ μmol $CO^{-1}$) |
|---|---|---|
| Pt/γ-$Al_2O_3$ | 0.56 | $1.4 \times 10^{-2}$ |
| PtCo/γ-$Al_2O_3$ | 3.6 | $7.8 \times 10^{-2}$ |
| PtNi/γ-$Al_2O_3$ | 5.2 | $5.4 \times 10^{-2}$ |
| PtCu/γ-$Al_2O_3$ | 1.2 | $3.3 \times 10^{-2}$ |

### 3.5. Flow reactor studies

The 1,3-butadiene conversion and product yields obtained from flow reactor studies are presented in Fig. 6a and b, respectively. The steady-state conversion and yields, at 180 min on stream, are included in Table 4. Fig. 6a shows the trend in conversion is PtCo/γ-$Al_2O_3$ > PtNi/γ-$Al_2O_3$ > Pt/γ-$Al_2O_3$ > PtCu/γ-$Al_2O_3$. Simi-

**Table 2**
Summary of Pt $L_{III}$-edge fitting for Pt/γ-$Al_2O_3$ and Pt3d/γ-$Al_2O_3$ bimetallic catalysts.

| Catalyst | Pt/γ-$Al_2O_3$ | PtCo/γ-$Al_2O_3$ | PtNi/γ-$Al_2O_3$ | PtCu/γ-$Al_2O_3$ |
|---|---|---|---|---|
| N(Pt–Pt) | 6.2 ± 0.4 | 4.7 ± 2.0 | 1.9 ± 0.5 | 3.4 ± 1.7 |
| N(Pt–Ni) | – | 3.3 ± 1.3 | 6.8 ± 0.3 | 6.3 ± 1.1 |
| R(Pt–Pt), Å | 2.75 ± 0.01 | 2.71 ± 0.01 | 2.67 ± 0.01 | 2.69 ± 0.02 |
| R(Pt–Ni), Å | – | 2.56 ± 0.02 | 2.55 ± 0.01 | 2.60 ± 0.01 |
| $\sigma^2$(Pt–Pt), Å$^2$ | 0.006 ± 0.001 | 0.006 ± 0.002 | 0.006 ± 0.001 | 0.008 ± 0.002 |
| $\sigma^2$(Pt–Ni), Å$^2$ | – | 0.008 ± 0.003 | 0.006 ± 0.001 | 0.007 ± 0.001 |

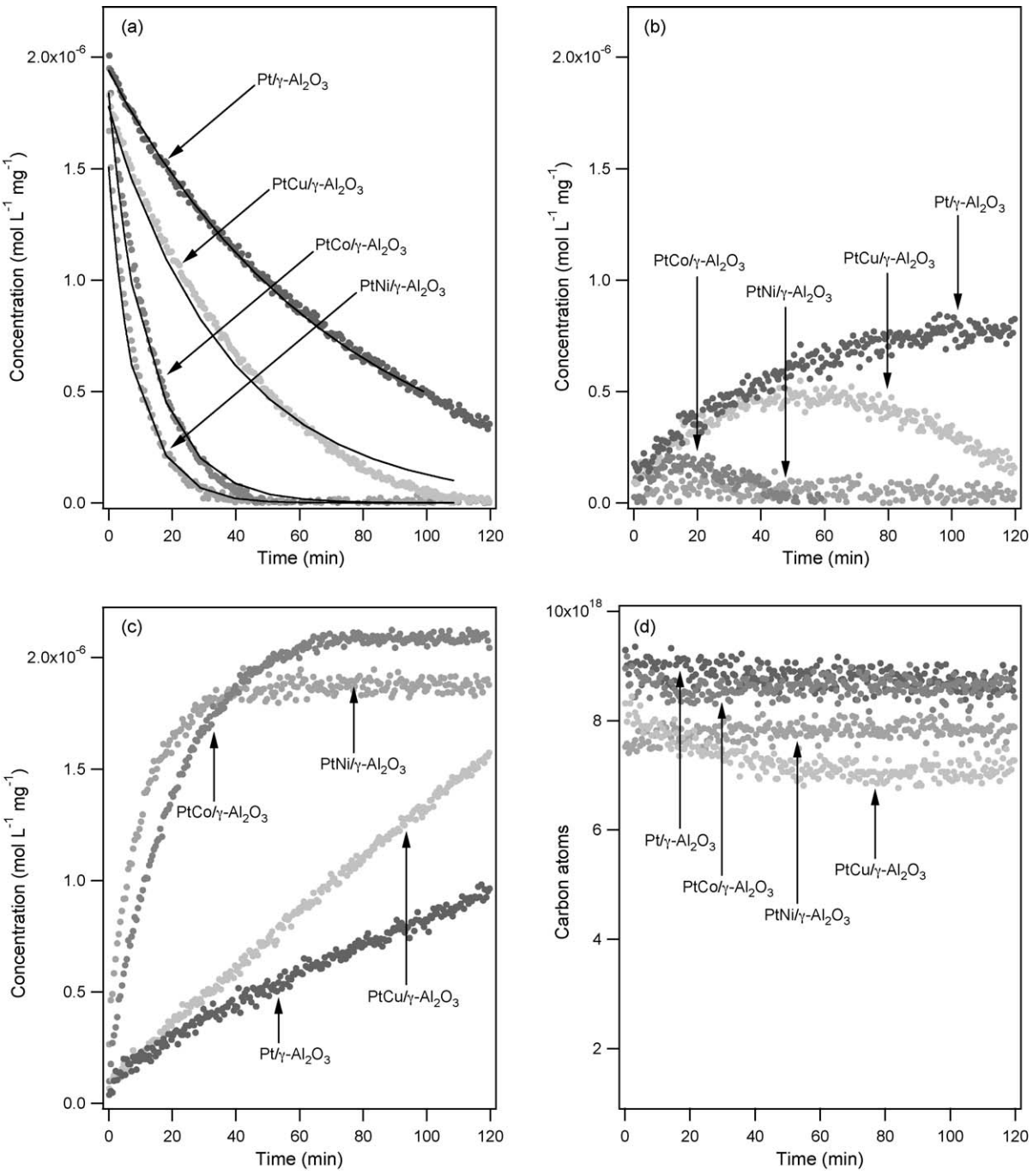


**Fig. 5.** Batch reactor hydrogenation of 1,3-butadiene: (a) consumption of 1,3-butadiene, (b) production and consumption of 1-butene, (c) production of n-butane, and (d) carbon balance of gas-phase species.

lar to the batch reactor studies (Table 3) both $PtCo/\gamma\text{-}Al_2O_3$ and $PtNi/\gamma\text{-}Al_2O_3$ display higher hydrogenation activity than the monometallic $Pt/\gamma\text{-}Al_2O_3$, however, $PtCu/\gamma\text{-}Al_2O_3$ displays lower activity than the monometallic catalyst.

The product yields in Fig. 6b show that $Pt/\gamma\text{-}Al_2O_3$ produces more 1-butene than n-butane, although the difference is small, and produces very small amounts of cis- and trans-2-butenes. Both $PtCo/\gamma\text{-}Al_2O_3$ and $PtNi/\gamma\text{-}Al_2O_3$ yield large amounts of n-butane,

**Table 4**
1,3-Butadiene hydrogenation product yields and ratios obtained from flow reactor studies.

| Catalyst | Yield (%) | | | | Product ratios | |
|---|---|---|---|---|---|---|
| | 1-Butene | Trans-2-butene | Cis-2-butene | n-Butane | Trans-2-butene/cis-2-butene | n-Butane/butenes |
| $Pt/\gamma\text{-}Al_2O_3$ | 1.7 | 0.29 | 0.54 | 1.1 | 1.9 | 0.43 |
| $PtCo/\gamma\text{-}Al_2O_3$ | 4.8 | 1.1 | 2.3 | 28 | 2.2 | 3.4 |
| $PtNi/\gamma\text{-}Al_2O_3$ | 1.6 | 0.47 | 0.98 | 24 | 2.1 | 7.9 |
| $PtCu/\gamma\text{-}Al_2O_3$ | 0.23 | 0.14 | 0.26 | 0 | 1.8 | 0 |

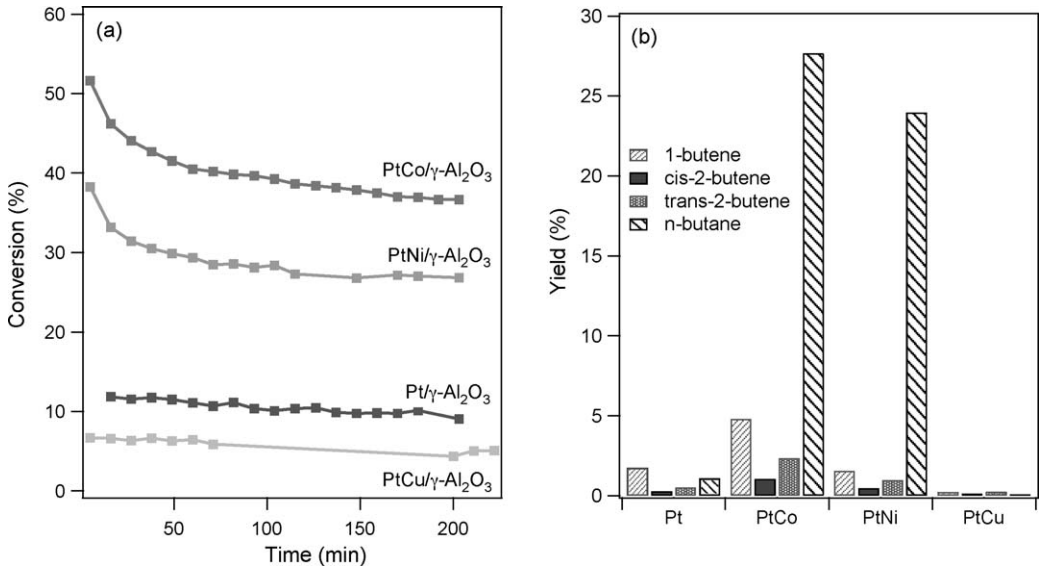


**Fig. 6.** Flow reactor hydrogenation of 1,3-butadiene: (a) 1,3-butadiene percent conversion and (b) product yields.

with 1-butene being the predominant butene product. PtCu/γ-$Al_2O_3$ displays relatively low hydrogenation activity in this study, but it appears to be selective to the production of butenes and no n-butane is detected in the product stream. Inspecting the ratios of the 2-butene isomers shown in Table 4, it is seen that for all four catalysts the ratio of trans-2-butene to cis-2-butene is fairly constant over all of the catalysts, ranging from 1.84 to 2.23. The ratio of n-butane to butenes shows that n-butane is the dominant hydrogenation product over PtCo/γ-$Al_2O_3$ and PtNi/γ-$Al_2O_3$, while the partial hydrogenation products, butenes, are preferred over PtCu/γ-$Al_2O_3$ and Pt/γ-$Al_2O_3$. The results from the flow and batch reactor studies show that both PtCo/γ-$Al_2O_3$ and PtNi/γ-$Al_2O_3$ are very active hydrogenation catalysts, however, their high hydrogenation activity makes them less selective toward the partial hydrogenation to produce butenes.

### 3.6. DFT calculations of binding energies

In previous studies the novel hydrogenation activity of Pt-based bimetallic catalysts has been correlated to weaker binding energies of alkenes on the bimetallic surfaces [17,18]. DFT calculations are performed in the current study to explore whether such correlation can be extended to conjugated molecules such as 1,3-butadiene. Fig. 7 shows the results of DFT calculations of the binding energies of 1,3-butadiene and atomic hydrogen on several Pt–3d–Pt(1 1 1) and 3d–Pt–Pt(1 1 1) surfaces. The binding energies are plotted versus the surface d-band center, which has been found to be a useful descriptor for the electronic properties of bimetallic surfaces [6]. Many research groups have been able to linearly correlate the binding energies of small molecules to the d-band center of various monometallic and bimetallic surfaces [9,21]. In Fig. 7, the binding energies of both 1,3-butadiene and hydrogen appear to correlate well to the d-band center, with binding energies being the weakest on the Pt–Co–Pt(1 1 1) and Pt–Ni–Pt(1 1 1) subsurface structures. In comparison, Co–Pt–Pt(1 1 1) and Ni–Pt–Pt(1 1 1) surface structures, with the surface d-band center being closest to the Fermi level among all the systems in Fig. 7, bind both adsorbates most strongly. It is also interest to note that, unlike other Pt/3d systems, the subsurface Pt–Cu–Pt(1 1 1) and surface Cu–Pt–Pt(1 1 1) structures bind 1,3-butadiene and hydrogen with very similar binding energies.

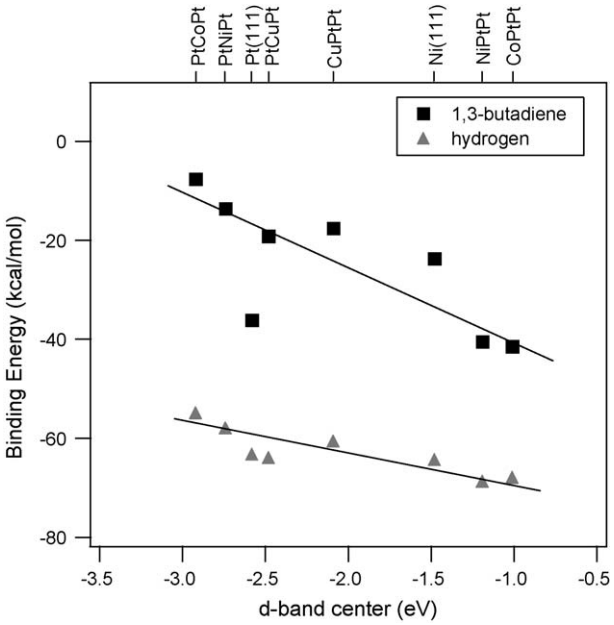


**Fig. 7.** DFT calculations of 1,3-butadiene and hydrogen binding energies as a function of d-band center.

## 4. Discussion

Previous work in correlating hydrogenation activity to d-band center has shown that surfaces that weakly bind atomic hydrogen and alkenes display greater hydrogenation activity [17,18]. This weak interaction between the surface and the adsorbate allows for the novel low-temperature hydrogenation to occur. The normalized rate constants obtained from batch reactor studies and the conversion obtained from flow reactor studies both show PtCo/γ-$Al_2O_3$ to be the most active bimetallic catalyst, with PtNi/γ-$Al_2O_3$ being the second most active, for 1,3-butadiene hydrogenation. Previous studies on supported bimetallic catalysts have shown that after reduction, the surface of Pt/Ni catalysts are composed of primarily Pt atoms [28,29], suggesting that the nanoparticle structure may more closely resemble the Pt–Ni–Pt subsurface

configuration than Ni–Pt–Pt. The presence of nanoparticle structures similar to the Pt–3d–Pt configuration would explain the higher activity observed on the PtCo/γ-$Al_2O_3$ and PtNi/γ-$Al_2O_3$ catalysts. Using the correlation between d-band center and binding energy shown in Fig. 7 to predict hydrogenation activity, the Pt–Co–Pt(1 1 1) structure should show the greatest activity followed by the Pt–Ni–Pt(1 1 1) structure, as verified by both the batch and flow reactor results.

However, based on the binding energies Fig. 7 also predicts that Pt–Cu–Pt(1 1 1) and Cu–Pt–Pt(1 1 1) should display greater hydrogenation activity than Pt(1 1 1). In the batch reactor studies the PtCu/γ-$Al_2O_3$ catalyst indeed shows higher activity than Pt/γ-$Al_2O_3$, but in the flow reactor studies it displays lower activity than Pt/γ-$Al_2O_3$. One possible explanation for this disagreement between theory and experiment can be explained by considering the thermodynamic stability of the surface and subsurface Pt/Cu structures. Fig. 7 shows that Pt–Cu–Pt(1 1 1) and Cu–Pt–Pt(1 1 1) bind 1,3-butadiene and hydrogen at very similar energies, suggesting that both configurations may be stable in the nanoparticles after reduction in hydrogen. The change in the surface configuration in PtCu/γ-$Al_2O_3$ probably happens more quickly in the flow reactor studies because the reaction pressure in the flow reactor, and therefore the number of adsorbed molecules, is much greater than that in the batch reactor (atmospheric pressure versus ~13 Torr). The segregation and diffusion of surface atoms might lead the adsorption of surface species that are not present on the other three catalysts. These surface species might reduce the hydrogenation activity of the PtCu/γ-$Al_2O_3$ catalyst, in particular in the flow reactor due to the higher pressure; the presence of surface species is also consistent with the observation of a relatively poor carbon balance in the batch reactor studies. Despite its low activity, the PtCu/γ-$Al_2O_3$ catalyst displays a preference toward partial hydrogenation to produce butenes. More detailed studies are necessary to understand the surface structure and the origin of the partial hydrogenation activity of this interesting bimetallic catalyst.

## 5. Conclusions

In the current paper we used the hydrogenation of 1,3-butadiene to demonstrate the importance of combining advanced characterization techniques and DFT calculations with catalytic studies. Three Pt/3d-metal bimetallic catalysts were synthesized in order to identify active hydrogenation catalysts. PtCo/γ-$Al_2O_3$ and PtNi/γ-$Al_2O_3$ catalysts were found to display hydrogenation activity greater than that of Pt/γ-$Al_2O_3$ in both batch and flow reactor studies. The observed activity over the PtCo/γ-$Al_2O_3$ and PtNi/γ-$Al_2O_3$ catalysts agrees well with DFT results which predict that the Pt–Co–Pt(1 1 1) and Pt–Ni–Pt(1 1 1) structures are good hydrogenation catalysts since they bind hydrogen and 1,3-butadiene more weakly than either Pt(1 1 1). The enhanced hydrogenation activity observed over the PtCo/γ-$Al_2O_3$ and PtNi/γ-$Al_2O_3$ catalysts suggests that the nanoparticle structure may be similar to the Pt–3d–Pt subsurface configurations identified in surface science and theoretical calculations. The PtCu/γ-$Al_2O_3$ catalyst shows a lower hydrogenation activity than the other bimetallic catalysts in the batch reactor, while it displays an activity even lower than Pt/γ-$Al_2O_3$ in the flow reactor studies. On the other hand, among the catalysts studied PtCu/γ-$Al_2O_3$ shows the best selectivity toward the partial hydrogenation to produce butenes in both batch and flow reactor studies.

## Acknowledgements

This work was supported as part of the Catalysis Center for Energy Innovation, an Energy Frontier Research Center funded by the US Department of Energy, Office of Basic Energy Sciences under Award Number DE-SC0001004. Use of the National Synchrotron Light Source, Brookhaven National Laboratory, for the EXAFS experiments was supported by the US Department of Energy, Office of Basic Energy Sciences (Grant# DE-FG02-05ER15688). The authors would like to thank Weiting Yu for her assistance with the DFT calculations. Suitao Qi and Xianjie Xing acknowledge support from the Chinese Ministry of Education for a visiting scholar program.

## References

[1] J.H. Sinfelt, Bimetallic Catalysts: Discoveries, Concepts, and Applications, Wiley, New York, 1983.
[2] J.A. Rodriguez, Surf. Sci. Rep. 24 (1996) 225.
[3] G.W. Huber, J.W. Shabaker, S.T. Evans, J.A. Dumesic, Appl. Catal. B: Environ. 62 (2006) 226.
[4] N.M. Markovic, P.N. Ross, Surf. Sci. Rep. 45 (2002) 121.
[5] E. Iglesia, S.L. Soled, R.A. Fiato, G.H. Via, J. Catal. 143 (1993) 345.
[6] J.G. Chen, C.A. Menning, M.B. Zellner, Surf. Sci. Rep. 63 (2008) 201.
[7] B. Hammer, J.K. Nørskov, Surf. Sci. 343 (1995) 211.
[8] D.W. Goodman, J. Phys. Chem. US 100 (1996) 13090.
[9] B. Hammer, J.K. Norskov, Adv. Catal. 45 (2000) 71.
[10] M. Neurock, V. Pallassana, R.A. van Santen, J. Am. Chem. Soc. 122 (2000) 1150.
[11] Y. Xu, A.V. Ruban, M. Mavrikakis, J. Am. Chem. Soc. 126 (2004) 4717.
[12] J. Greeley, M. Mavrikakis, Nat. Mater. 3 (2004) 810.
[13] H.H. Hwu, J. Eng, J.G. Chen, J. Am. Chem. Soc. 124 (2002) 702.
[14] N.A. Khan, H.H. Hwu, J.G. Chen, J. Catal. 205 (2002) 259.
[15] J.R. Kitchin, N.A. Khan, M.A. Barteau, J.G. Chen, B. Yakshinksiy, T.E. Madey, Surf. Sci. 544 (2003) 295.
[16] O. Skoplyak, M.A. Barteau, J.G. Chen, J. Phys. Chem. B 110 (2006) 1686.
[17] M.P. Humbert, J.G. Chen, J. Catal. 257 (2008) 297.
[18] N.A. Khan, L.E. Murillo, J.G. Chen, J. Phys. Chem. B 108 (2004) 15748.
[19] C.A. Menning, H.H. Hwu, J.G. Chen, J. Phys. Chem. B 110 (2006) 15471.
[20] L.E. Murillo, C.A. Menning, J.G. Chen, J. Catal. 268 (2009) 335.
[21] J.R. Kitchin, J.K. Norskov, M.A. Barteau, J.G. Chen, J. Chem. Phys. 120 (2004) 10240.
[22] C.A. Menning, J.G. Chen, J. Chem. Phys. 130 (2009) 174709.
[23] O. Skoplyak, C.A. Menning, M.A. Barteau, J.G. Chen, Top. Catal. 51 (2008) 49.
[24] L.E. Murillo, A.M. Goda, J.G. Chen, J. Am. Chem. Soc. 129 (2007) 7101.
[25] O. Skoplyak, M.A. Barteau, J.G. Chen, ChemSusChem 1 (2008) 524.
[26] C.A. Menning, J.G. Chen, J. Chem. Phys. 128 (2008) 164703.
[27] C.A. Menning, J.G. Chen, J. Power Sources 195 (2010) 3140.
[28] R.T. Mu, Q. Fu, H.Y. Liu, D.L. Tan, R.S. Zhai, X.H. Bao, Appl. Surf. Sci. 255 (2009) 7296.
[29] W.W. Lonergan, D.G. Vlachos, J.G. Chen, J. Catal. (2010).
[30] D. Seth, A. Sarkar, F.T.T. Ng, G.L. Rempel, Chem. Eng. Sci. 62 (2007) 4544.
[31] J. Goetz, D.Y. Murzin, M. Ulischenko, R. Touroude, Chem. Eng. Sci. 51 (1996) 2879.
[32] M. Benkhaled, C. Descorme, D. Duprez, S. Morin, C. Thomazeau, D. Uzio, Appl. Catal. A: Gen. 346 (2008) 36.
[33] J. Silvestre-Albero, G. Rupprechter, H.J. Freund, J. Catal. 240 (2006) 58.
[34] J.C. Bertolini, Appl. Catal. A: Gen. 191 (2000) 15.
[35] A. Sarkany, G. Stefler, J.W. Hightower, Appl. Catal. A: Gen. 127 (1995) 77.
[36] A. Valcarcel, A. Clotet, J.M. Ricart, F. Delbecq, P. Sautet, Surf. Sci. 549 (2004) 121.
[37] M. Newville, J. Synchrotron Radiat. 8 (2001) 96.
[38] B. Ravel, M. Newville, J. Synchrotron Radiat. 12 (2005) 537.
[39] J.J. Rehr, R.C. Albers, Rev. Mod. Phys. 72 (2000) 621.
[40] P. Basu, T.H. Ballinger, J.T. Yates, Rev. Sci. Instrum. 59 (1988) 1321.
[41] G. Kresse, J. Furthmuller, Phys. Rev. B 54 (1996) 11169.
[42] G. Kresse, J. Furthmuller, Comp. Mater. Sci. 6 (1996) 15.
[43] G. Kresse, J. Hafner, Phys. Rev. B 47 (1993) 558.
[44] J.P. Perdew, J.A. Chevary, S.H. Vosko, K.A. Jackson, M.R. Pederson, D.J. Singh, C. Fiolhais, Phys. Rev. B 46 (1992) 6671.
[45] M.P. Teter, M.C. Payne, D.C. Allan, Phys. Rev. B 40 (1989) 12255.
[46] A. Jentys, B.J. Mchugh, G.L. Haller, J.A. Lercher, J. Phys. Chem. 96 (1992) 1324.
[47] A.I. Frenkel, C.W. Hills, R.G. Nuzzo, J. Phys. Chem. B 105 (2001) 12689.